JOURNAL OF COMPUTATIONAL PHYSICS 101, 276–286 (1992)

Three-Dimensional Calculations of Supersonic Reacting Flows Using an LU Scheme

SHENG-TAO YU, Y.-L. PETER TSAI, AND JIAN-SHUN SHUEN

Sverdrup Technology, Inc., NASA Lewis Research Center, Cleveland, Ohio 44135

Received August 7, 1989; revised July 8, 1991

A new three-dimensional numerical program that incorporates comprehensive real gas property models has been developed to simulate supersonic reacting flows. The code employs an implicit, finite volume, Lower–Upper (LU), time-marching method to solve the complete Navier–Stokes and species equations in a fully coupled and very efficient manner. A chemistry model with nine species and eighteen reaction steps is adopted in the program to represent the chemical reactions of H_2 an air. To demonstrate the capability of the program, flow fields of underexpanded hydrogen jets transversely injected into the supersonic airstream inside the combustors of scramjets are calculated. Results clearly depict the flow characteristics, including the shock structure, the separated flow regions around the injector, and the distribution of the combustion products.

INTRODUCTION

Recent developments in hypersonic, air-breating vehicles have stimulated attempts to apply numerical methods to simulate related flow fields. The objective of the present research is to develop a three-dimensional fluid dynamic code for studying mixing and chemically reacting flows inside supersonic combustion ramjet (scramjet) engine.

The LU numerical scheme adopted in the present research [1] is formulated based upon eigenvalue upwinding. This method has the efficiency and robustness of an implicit scheme, with an operational count comparable to that of an explicit scheme. This special feature of the LU scheme is very important for three-dimensional calculations of large systems of equations for chemically reacting flows. In this paper, the capability and advantages of the LU scheme as well as the vectorization strategy are elaborated.

Previously, a two-dimensional computer code using an LU scheme has been developed [2, 3]. This program is capable of simulating chemical reacting flows with finite rate or equilibrium chemistry. We have used it to simulate the flow field of the combustion of a hydrogen jet transversely injected into a supersonic airstream [2] as well as hypersonic inlet flows at Machs 10 and 13 [3]. Results predicted by the two-dimensional code compared favorably with the experimental data and other numerical solutions. In this paper, the two-dimensional code is extended to three dimensions. As shown in the following sections, the advantage of the LU scheme is greatly magnified in the three-dimensional flows.

As numerical examples, the flow fields of a hydrogen jet interacting with a supersonic cross airstream are calculated. First, the code was applied to simulate McDaniel's experiment [4], which was a non-reacting mixing flow field. The predicted results compare favorably with experimental data in terms of the penetration depth of the fuel injection. Then, the chemical reacting flows of single-injection and dual-injection into cross airstream are calculated. The finite rate chemistry model adopted involves nine chemical species with eighteen reaction steps. Because of the efficiency of the LU scheme, the three-dimensional calculation for chemically reacting flows is well within the current computer capability.

ANALYSIS

For three-dimensional chemical reacting flows with N_s species, the governing equations can be cast into vector form in Cartesian coordinates as

$$\frac{\partial Q}{\partial t}+\frac{\partial}{\partial x}(E-E_v)+\frac{\partial}{\partial y}(F-F_v)+\frac{\partial}{\partial z}(G-G_v)=H \quad (1)$$

where

$$Q=\begin{pmatrix}\rho\\ \rho u\\ \rho v\\ \rho w\\ \rho e\\ \rho Y_i\end{pmatrix} \quad (2)$$

0021-9991/92 $5.00

$$E=\begin{pmatrix}\rho u\\ \rho u^2+p\\ \rho uv\\ \rho uw\\ u(\rho e+p)\\ \rho uY_i\end{pmatrix} \quad (3)$$

$$F=\begin{pmatrix}\rho v\\ \rho uv\\ \rho v^2+p\\ \rho vw\\ v(\rho e+p)\\ \rho vY_i\end{pmatrix} \quad (4)$$

$$G=\begin{pmatrix}\rho w\\ \rho uw\\ \rho vw\\ \rho w^2+p\\ w(\rho e+p)\\ \rho wY_i\end{pmatrix} \quad (5)$$

$$E_v=\begin{pmatrix}0\\ \tau_{xx}\\ \tau_{xy}\\ \tau_{xz}\\ u\tau_{xx}+v\tau_{xy}+w\tau_{zx}-q_x\\ -\rho\hat{u}_iY_i\end{pmatrix} \quad (6)$$

$$F_v=\begin{pmatrix}0\\ \tau_{xy}\\ \tau_{yy}\\ \tau_{yz}\\ u\tau_{xy}+v\tau_{yy}+w\tau_{yz}-q_y\\ -\rho\hat{v}_iY_i\end{pmatrix} \quad (7)$$

$$G_v=\begin{pmatrix}0\\ \tau_{zx}\\ \tau_{yz}\\ \tau_{zz}\\ u\tau_{zx}+v\tau_{yz}v+w\tau_{zz}-q_z\\ -\rho\hat{w}_iY_i\end{pmatrix} \quad (8)$$

and

$$H=\begin{pmatrix}0\\ 0\\ 0\\ 0\\ 0\\ \dot{\omega}_i\end{pmatrix} \quad (9)$$

$i=1, 2, 3, ..., N_s-1,$

where ρ is the density, and u, v, and w are the velocity components in the x, y, and z directions, respectively. Here p is the pressure and e is the specific total energy, which is defined as

$$e=\sum_{i=1}^{N_s}Y_ie_i+\tfrac{1}{2}(u^2+v^2+w^2), \quad (10)$$

where Y_i and e_i are the mass fraction and specific internal energy for species i. τ_{xy}, τ_{yz}, τ_{zx}, τ_{xx}, τ_{yy}, and τ_{zz} are shear and normal stresses. Because the summation of the mass fractions of all the chemical species is one, only N_s-1 species equations need to be solved. In the energy equation, q_x, q_y, and q_z represent the energy fluxes due to heat conduction and species diffusion. They can be expressed as

$$\begin{aligned}q_x&=-k\frac{\partial T}{\partial x}+\rho\sum_{i=1}^{N_s}h_iY_i\hat{u}_i\\ q_y&=-k\frac{\partial T}{\partial y}+\rho\sum_{i=1}^{N_s}h_iY_i\hat{v}_i\\ q_z&=-k\frac{\partial T}{\partial z}+\rho\sum_{i=1}^{N_s}h_iY_i\hat{w}_i,\end{aligned} \quad (11)$$

where h_i is the enthalpy of species i. The diffusion velocity components, $\hat{u}_i$, $\hat{v}_i$, and $\hat{w}_i$ are calculated by Fick's law [5],

$$\begin{aligned}Y_i\hat{u}_i&=-D_{im}\frac{\partial Y_i}{\partial x}\\ Y_i\hat{v}_i&=-D_{im}\frac{\partial Y_i}{\partial y}\\ Y_i\hat{w}_i&=-D_{im}\frac{\partial Y_i}{\partial z},\end{aligned} \quad (12)$$

where

$$D_{im}=(1-X_i)\Big/\sum_{i\neq j}\frac{X_i}{D_{ij}} \quad (13)$$

is the effective binary diffusivity of species i in the gas mixture and X_i is the mole fraction of species i.

The pressure and temperature are calculated interatively from the equations

$$e=\sum_{i=1}^{N_s}Y_ih_i-\frac{p}{\rho}+\frac{1}{2}(u^2+v^2+w^2) \quad (14)$$

$$h_i=h_{fi}^0+\int_{T_{ref}}^{T}C_{pi}\,dT \quad (15)$$

$$p=\rho R_uT\sum_{i=1}^{N_s}\frac{Y_i}{W_i}, \quad (16)$$

where h_{fi}^0 is the heat of formation of species i, C_{pi} is the constant pressure specific heat of species i, and W_i the molecular weight of species i. Equation (16) is the equation of state for a gas mixture of N_s species.

The constant pressure specific heat C_p, thermal conductivity, viscosity, and diffusivity for each species are determined by fourth order polynomials of temperature, such as

$$k_i = a_0 + a_1 T + a_2 T^2 + a_3 T^3 + a_4 T^4. \tag{17}$$

The coefficients of these polynomials are supplied by Gordon and McBride and are valid up to a temperature of 6000 K [6]. The specific heat of the gas mixture is obtained by mass concentration weighting. The thermal conductivity and viscosity of the gas mixture are calculated using Wilke's mixing rule [7]. The binary mass diffusivity between species is obtained using the Chapman–Enskog theory in conjunction with the Lennard–Jones intermolecular potential energy functions [7].

As noted in Eq. (9), the right hand side of the species equations contains source terms ($\dot{\omega}_i$). These terms represent the generation or destruction of species i due to chemical reactions. The stochiometric equation of a set of N_R elementary reactions involving N_s species is

$$\sum_{i=1}^{N_s} \nu'_{ij} C_i \underset{K_{b_j}}{\overset{K_{f_j}}{\rightleftharpoons}} \sum_{i=1}^{N_s} \nu''_{ij} C_i, \qquad j = 1, 2, \ldots, N_R, \tag{18}$$

where C_i is the mole concentration of species i. K_{f_j} and K_{b_j} are reaction rate constants and are given by the Arrhenius form [5]

$$K_{f_j} = A_{f_j} T^{B_{f_j}} e^{-E_{f_j}/RT}$$
$$K_{b_j} = A_{b_j} T^{B_{b_j}} e^{-E_{b_j}/RT}. \tag{19}$$

The rate of change of species i by reaction j is

$$(\dot{C}_i)_j = (\nu''_{ij} - \nu'_{ij}) \left(K_{f_j} \prod_{i=1}^{N_s} C_i^{\nu'_{ij}} - K_{b_j} \prod_{i=1}^{N_s} C_i^{\nu''_{ij}} \right). \tag{20}$$

The total rate of change of species i is

$$\dot{\omega}_i = W_i \sum_{j=1}^{N_R} (\dot{C}_i)_j. \tag{21}$$

The energy equation has no source term because both the sensible energy and the heat of formation of each species are included in the total energy (e) and the enthalpy (h_i) (Eqs. (14) and (15)).

In the present study, a nine-species and eighteen step chemistry is adopted. These species include H_2, H, OH, H_2O, O, O_2, HO_2, H_2O_2, and N_2. This model is a reduced H_2-air reaction system developed by Brabbs [8]. For turbulent flows, the closure of the governing equations is provided by the Baldwin–Lomax model [9] and constant turbulent Prandtl and Schmidt numbers ($Pr_t = Sc_t = 0.9$). This model is chosen for its simplicity and computational efficiency.

NUMERICAL METHOD

The LU scheme adopted in the present study was originally developed by Yoon and Jameson [1]. In deriving the discretized counterpart of the governing equations, Yoon and Jameson proposed using backward and forward relaxation sweeps in the diagonal directions to invert the implicit operator and obtained the Lower–Upper Symmetric Successive Overrelaxation (LU-SSOR) scheme. In this paper, a different derivation procedure is taken. The linearized governing equations are

$$\frac{\partial Q}{\partial t} + \frac{\partial}{\partial x}(E^n + A^n \Delta Q) + \frac{\partial}{\partial y}(F^n + B^n \Delta Q) + \frac{\partial}{\partial z}(G^n + C^n \Delta Q) = \frac{\partial E_v^n}{\partial x} + \frac{\partial F_v^n}{\partial y} + \frac{\partial G_v^n}{\partial z} + H^n + T^n \Delta Q, \tag{22}$$

where the Jacobian matrices A, B, C, and T are defined as

$$A = \frac{\partial E}{\partial Q}, \quad B = \frac{\partial F}{\partial Q}, \quad C = \frac{\partial G}{\partial Q}, \quad T = \frac{\partial H}{\partial Q}, \tag{23}$$

and the superscript n denotes the time step. Note that the source terms of the species equations in finite rate calculations are treated implicitly. According to Bussing and Murman [10], treating the source terms implicitly is equivalent to rescaling the characteristic times of the governing equations and thus stabilizing the numerical calculations. Viscous terms in Eq. (22) are not linearized and are treated explicitly to reduce complexity.

In deriving the Jacobian matrices A, B, and C, it is necessary to evaluate the derivatives with respect to other unknown variables. For perfect gas, this procedure is rather straight forward due to the usage of the relations $h = C_p T$ and $C_p/C_v = \gamma$, where C_p and γ are both constants. For reacting flows, the species composition of the gas mixture varies spatially and the specific heats (C_p and C_v) of each species are functions of temperature. Thus, special treatment must be adopted in obtaining the pressure derivatives. A simple

remedy is to use the so-called "equivalent specific heat ratio ($\hat{\gamma}$)" [11],

$$\hat{\gamma} = \frac{h_{sm}}{e_{sm}} = \frac{\sum_{i=1}^{N_s} Y_i \int_0^T C_{p_i}\, dt}{\sum_{i=1}^{N_s} Y_i \int_0^T C_{v_i}\, dt} \tag{24}$$

where h_{sm} and e_{sm} are the sensible enthalpy and internal energy of the gas mixture, respectively. In general, $\hat{\gamma}$ is function of both thermodynamic and flow properties. However, Colella and Glaz [12] had shown that this function varies very slowly with respect to other properties. Thus, $\hat{\gamma}$ is treated as a local constant. By this assumption, we obtain the expression of pressure,

$$p = (\hat{\gamma}-1)\,\rho e_{sm} = (\hat{\gamma}-1)\left[\rho e - \rho h^0_{fm} - \frac{\rho}{2}(u^2+v^2+w^2)\right] \tag{25}$$

where $h^0_{fm} = \sum Y_i (h^0_{f_i} - \int_0^{T_{ref}} C_{p_i}\, dt)$. Since only $N_s - 1$ species equations are actually solved, Eq. (25) needs to be rearranged to the form

$$\begin{aligned} p &= (\hat{\gamma}-1)\left[\rho e - \sum_{i=1}^{N_s-1} \rho Y_i h^0_{fi} - \left(\rho - \sum_{i=1}^{N_s-1} \rho Y_i\right) h^0_{f_{N_s}} - \frac{\rho}{2}(u^2+v^2+w^2)\right] \\ &= (\hat{\gamma}-1)\left[\rho e - \rho h^0_{f_{N_s}} - \sum_{i=1}^{N_s-1} \rho Y_i\, \delta h^0_{fi} - \frac{\rho}{2}(u^2+v^2+w^2)\right], \end{aligned} \tag{26}$$

where $\delta h^0_{fi} = h^0_{fi} - h^0_{f_{N_s}}$. The final form of the Jacobian matrix A is,

$$A = \begin{bmatrix} 0 & 1 & 0 & 0 & 0 & 0 & \cdots & 0 \\ -u_2 + (\hat{\gamma}-1)\left(\frac{q^2}{2} - h^0_{f_{N_s}}\right) & (3-\hat{\gamma})u & (1-\hat{\gamma})v & (1-\hat{\gamma})w & (\hat{\gamma}-1) & (1-\hat{\gamma})\,\delta h^0_{f_1} & \cdots & (1-\hat{\gamma})\,\delta h^0_{f_{N_s-1}} \\ -uv & v & u & 0 & 0 & 0 & \cdots & 0 \\ -uw & w & 0 & u & 0 & 0 & \cdots & 0 \\ -(\rho e + p)\frac{u}{\rho} + & (\rho e + P)/\rho - & (1-\hat{\gamma})\,uv & (1-\hat{\gamma})\,uw & u\hat{\gamma} & (1-\hat{\gamma})\,u\,\delta h^0_{f_1} & \cdots & (1-\hat{\gamma})\,u\,\delta h^0_{f_{N_s-1}} \\ u(\hat{\gamma}-1)\left(\frac{q^2}{2} - h^0_{f_{N_s}}\right) & u^2(\hat{\gamma}-1) & & & & & & \\ uY_1 & Y_1 & 0 & 0 & 0 & u & \cdots & 0 \\ \cdot & \cdot & \cdot & \cdot & \cdot & \cdot & \cdots & \cdot \\ \cdot & \cdot & \cdot & \cdot & \cdot & \cdot & \cdots & \cdot \\ \cdot & \cdot & \cdot & \cdot & \cdot & \cdot & \cdots & \cdot \\ uY_{N_s-1} & Y_{N_s-1} & 0 & 0 & 0 & 0 & \cdots & u \end{bmatrix}, \tag{27}$$

where $q^2 = u^2 + v^2 + w^2$. The form of the matrices B and C are similar to that of A. The Jacobian matrix T represents implicit treatment of the chemical source terms and is of the form

$$T = \begin{bmatrix} 0 & 0 & 0 & 0 & 0 & 0 & \cdots & 0 \\ 0 & 0 & 0 & 0 & 0 & 0 & \cdots & 0 \\ 0 & 0 & 0 & 0 & 0 & 0 & \cdots & 0 \\ 0 & 0 & 0 & 0 & 0 & 0 & \cdots & 0 \\ 0 & 0 & 0 & 0 & 0 & 0 & \cdots & 0 \\ \frac{\partial \dot{\omega}_1}{\partial \rho} & \frac{\partial \dot{\omega}_1}{\partial \rho u} & \frac{\partial \dot{\omega}_1}{\partial \rho v} & \frac{\partial \dot{\omega}_1}{\partial \rho w} & \frac{\partial \dot{\omega}_1}{\partial \rho e} & \frac{\partial \dot{\omega}_1}{\partial \rho Y_1} & \cdots & \frac{\partial \dot{\omega}_1}{\partial \rho Y_{N_s-1}} \\ \cdot & \cdot & \cdot & \cdot & \cdot & \cdot & \cdots & \cdot \\ \cdot & \cdot & \cdot & \cdot & \cdot & \cdot & \cdots & \cdot \\ \cdot & \cdot & \cdot & \cdot & \cdot & \cdot & \cdots & \cdot \\ \frac{\partial \dot{\omega}_{N_s-1}}{\partial \rho} & \frac{\partial \dot{\omega}_{N_s-1}}{\partial \rho u} & \frac{\partial \dot{\omega}_{N_s-1}}{\partial \rho v} & \frac{\partial \dot{\omega}_{N_s-1}}{\partial \rho w} & \frac{\partial \dot{\omega}_{N_s-1}}{\partial \rho e} & \frac{\partial \dot{\omega}_{N_s-1}}{\partial \rho Y_1} & \cdots & \frac{\partial \dot{\omega}_{N_s-1}}{\partial \rho Y_{N_s-1}} \end{bmatrix}. \tag{28}$$

In the actual coding, $\partial\dot{\omega}_i/\partial\rho$, $\partial\dot{\omega}_i/\partial\rho u$, $\partial\dot{\omega}_i/\partial\rho v$, and $\partial\dot{\omega}_i/\partial\rho w$ are taken as zero since they are usually small. However, for combustion under extreme condition, e.g., detonation wave, it is necessary to include these terms. The terms $\partial\dot{\omega}_i/\partial\rho Y_i$ can be readily obtained through Eqs. (20) and (21).

For the lower and upper splitting, let

$$\begin{aligned} A &= A^+ + A^- \\ B &= B^+ + B^- \\ C &= C^+ + C^-, \end{aligned} \tag{29}$$

where A^+, A^-, B^+, B^-, C^+, and C^- are constructed such that the eigenvalues of the matrices have the same sign as the superscripts. Of the many ways of splitting the Jacobian matrices, Jameson and Turkel's method [13] is adopted,

$$\begin{aligned} A^+ &= 0.5(A + \gamma_A I) \\ A^- &= 0.5(A - \gamma_A I), \end{aligned} \tag{30}$$

where

$$\gamma_A \geqslant \max(|\lambda_A|). \tag{31}$$

Here λ_A is the maximum eigenvalue of Jacobian matrices A. Substituting Eq. (29) into Eq. (22) and performing the first order upwinding difference according to the sign of the eigenvalues gives the equation

$$\begin{aligned} [I + \Delta t(D_x^- A^+ + D_x^+ A^- + D_y^- B^+ + D_y^+ B^- \\ + D_z^- C^+ + D_z^+ C^- - T)]\,\Delta Q = \Delta t\ \text{RHS}, \end{aligned} \tag{32}$$

where D_x^+, D_y^+, and D_z^+ are forward-difference operators, and D_z^-, D_y^-, and D_z^- are backward-difference operators. In Eq. (32),

$$\begin{aligned} \text{RHS} = &-\frac{\partial E^n}{\partial x} - \frac{\partial F^n}{\partial y} - \frac{\partial G^n}{\partial z} \\ &+ \frac{\partial E_v^n}{\partial x} + \frac{\partial F_v^n}{\partial y} + \frac{\partial G_v^n}{\partial z} + H^n. \end{aligned} \tag{33}$$

Equation (32) can be expanded in discretized form to produce

$$\begin{aligned} &N\,\Delta Q_{ijk} - \Delta t\, T_{ijk}\,\Delta Q_{ijk} \\ &\quad + \frac{\Delta t}{\Delta x}(A^-_{i+1,j,k}\,\Delta Q_{i+1,j,k} - A^+_{i-1,j,k}\,\Delta Q_{i-1,j,k}) \\ &\quad + \frac{\Delta t}{\Delta y}(B^-_{i,j+1,k}\,\Delta Q_{i,j+1,k} - B^+_{i,j-1,k}\,\Delta Q_{i,j-1,k}) \\ &\quad + \frac{\Delta t}{\Delta z}(C^-_{i,j,k+1}\,\Delta Q_{i,j,k+1} - C^+_{i,j,k-1}\,\Delta Q_{i,j,k-1}) \\ &= \Delta t\ \text{RHS}, \end{aligned} \tag{34}$$

where N includes all the diagonal terms except the matrix T and can be expressed as

$$\begin{aligned} N = I &+ \frac{\Delta t}{\Delta x}(A^+_{i,j,k} - A^-_{i,j,k}) + \frac{\Delta t}{\Delta y}(B^+_{i,j,k} - B^-_{i,j,k}) \\ &+ \frac{\Delta t}{\Delta z}(C^+_{i,j,k} - C^-_{i,j,k}). \end{aligned} \tag{35}$$

Equation (34) can be approximately factorized depending on the sign of the Jacobian matrices:

$$\begin{aligned} &\left[N + \frac{\Delta t}{\Delta x}(A^-_{i+1,j,k}) + \frac{\Delta t}{\Delta y}(B^-_{i,j+1,k}) + \frac{\Delta t}{\Delta z}(C^-_{i,j,k+1})\right] N^{-1} \\ &\left[N - \Delta t\, T_{i,j} - \frac{\Delta t}{\Delta x}(A^+_{i-1,j,k}) \right. \\ &\qquad \left. - \frac{\Delta t}{\Delta y}(B^+_{i,j-1,k}) - \frac{\Delta t}{\Delta z}(C^+_{i,j,k-1})\right]\Delta Q \\ &= \Delta t\ \text{RHS}. \end{aligned} \tag{36}$$

Note that matrix N is diagonal. This can easily be verified by substituting Eq. (30) into the definition of N [Eq. (35)]

$$N = \left(1 + \frac{\Delta t}{\Delta x}\gamma_A + \frac{\Delta t}{\Delta y}\gamma_B + \frac{\Delta t}{\Delta z}\gamma_C\right) I. \tag{37}$$

Thus, N^{-1} is also diagonal and can be moved to the right hand side of Eq. (36). One then obtains

$$\begin{aligned} &\left[I + \Delta t\left(D_x^+ A^- + D_y^+ B^- + D_z^+ C^- \right.\right. \\ &\qquad \left.\left. + \frac{A^+_{i,j,k}}{\Delta x} + \frac{B^+_{i,j,k}}{\Delta y} + \frac{C^+_{i,j,k}}{\Delta z}\right)\right] \\ &\left[I - \Delta t\, T + \Delta t\left(D_x^- A^+ + D_y^- B^+ + D_x^- C^+ \right.\right. \\ &\qquad \left.\left. - \frac{A^-_{i,j,k}}{\Delta x} - \frac{B^-_{i,j,k}}{\Delta y} - \frac{C^-_{i,j,k}}{\Delta z}\right)\right]\Delta Q \\ &= \left(1 + \frac{\Delta t}{\Delta x}\gamma_A + \frac{\Delta t}{\Delta y}\gamma_B + \frac{\Delta t}{\Delta z}\gamma_C\right)\Delta t\ \text{RHS}. \end{aligned} \tag{38}$$

Note that for non-reacting or chemical equilibrium calculations, there is no source term in the governing equations, and the matrix inversion is avoided without using the diagonalization technique. In fact, the two operators in Eq. (38) require only scalar inversions. For finite-rate chemistry calculations, the second operator of Eq. (38) requires a block diagonal inversion which resulted from the implicit treatment of the source terms. However, since the flow equations (the continuity, momentum, and energy

equations) have no source term, the first five rows of the second operator in Eq. (38) have nonzero terms only in the diagonal. Thus, for the chemically reacting flows, the second operator can be inverted in two separate steps: scalar diagonal inversions for the flow equations and block diagonal inversion for the species equations. In addition, the inclusion of the terms $\partial\dot{\omega}_i/\partial\rho u$, $\partial\dot{\omega}_i/\partial\rho v$, and $\partial\dot{\omega}_i/\partial\rho w$ in the matrix T does not change the aforementioned inversion procedure. After the scalar inversion of the flow equations, the extra terms can be readily moved to the right hand side before the block inversion proceeds.

The standard second order central difference is adopted for the discretization of the right hand side. Jameson's artificial damping [1] is used for the numerical stability. This artificial viscosity includes two parts: the second order and fourth order dampings. The fourth order one is applied to the whole flow field whereas the second order one is turned on whenever there is shock to prevent numerical oscillation caused by shock. Details of the artificial viscosity and stability analysis of the numerical scheme are provided in Ref. [13].

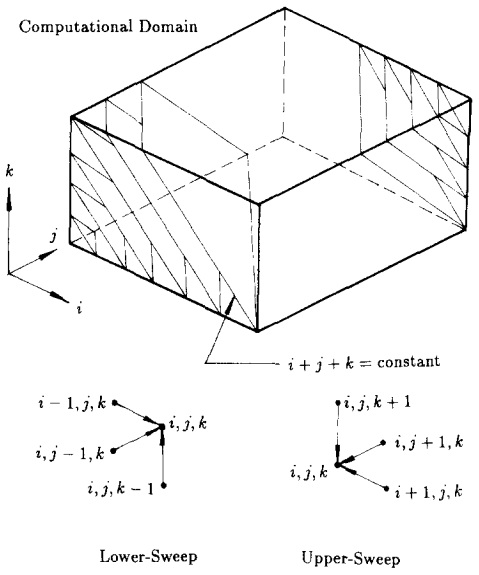

FIG. 1. Schematic of parallel-processing planes for the LU scheme.

PROGRAM VECTORIZATION

The newly developed three-dimensional program has been efficiently vectorized. Usually, implicit schemes cannot be vectorized as efficiently as explicit schemes because of the recursive property in solving the implicit operators. For instance, the well-known ADI scheme [14] requires inverting tridiagonal matrices in three directions. Such inversion involves forward and backward substitutions which are both recursive. In i-sweep, for example, the solution of a point (i, j, k) depends upon $(i-1, j, k)$ in forward substitution, and upon $(i+1, j, k)$ in backward substitution. However, points in a constant-i plane can be parallel-processed, and a program using the ADI scheme can be vectorized in two dimensions. The implicit operator of the LU scheme also has a recursive property. In the LU scheme, the solution of the point (i, j, k) requires updated values of points $(i-1, j, k)$, $(i, j-1, k)$, and $(i, j, k-1)$ in the Lower sweep; and updated values of $(i+1, j, k)$, $(i, j+1, k)$, and $(i, j, k+1)$ in the Upper sweep. Similar to the ADI scheme, points in a plane normal to the sweeping direction can be parallel-processed. The difference is the sweeping direction. For the LU scheme, the parallel-processing planes can be represented by a relation between the indices, $i+j+k=$ constant. The schematic of these planes for the Lower sweep is shown in Fig. 1. The vectorization of the LU-scheme program is also two-dimensional; however, the indices of the points in a parallel-processing plane are not as organized as those of the ADI scheme.

The program is vectorized by reorganizing the indices of the grid points for the parallel-processing planes. Before the main iteration begins, mappings between the three-dimensional index (i, j, k), and two sets of two-dimensional indices (*ipoint*, *iplane*), are generated for the Lower and Upper sweeps. The index *ipoint* identifies the points in a parallel-processing plane, and *iplane* identifies the planes. These mappings are stored as sets of integer arrays which can be invoked by L and U sweeps. On CRAY computers, the mapping arrays can be used directly in DO-loops to achieve efficient vectorization. On CDC/CYBER computers, vectorization is done by gathering and/or scattering the vector elements on the basis of the mapping arrays.

The efficiency of vectorization depends upon the strategy as well as the vector-processing architecture. Note that the strategy described results in short vectors near the Lower and Upper corners. For two reasons these inefficient vector-processing regions near the corners do not constitute a significant efficiency-reduction on the CRAY we use. First, the vector length becomes rapidly larger as the distance between the plane and the corners increases. (The vector length is approximately proportional to the square of the distance.) Second, CRAY's maximum computation speed can almost be reached with a rather short vector-length (e.g., 100). This property helps to reduce inefficient vector-processing regions. In fact, the CPU time for the implicit operator is reduced by a factor of nearly 10 simply by the described strategy. The vectorization of the RHS is relatively straightforward. In principle, three-dimensional vectorization is possible for the RHS. However, our experience on the CRAY shows very little difference among one-, two-, and three-dimensional vectorizations due to its architecture. The program is therefore vectorized in one dimension for better readability.

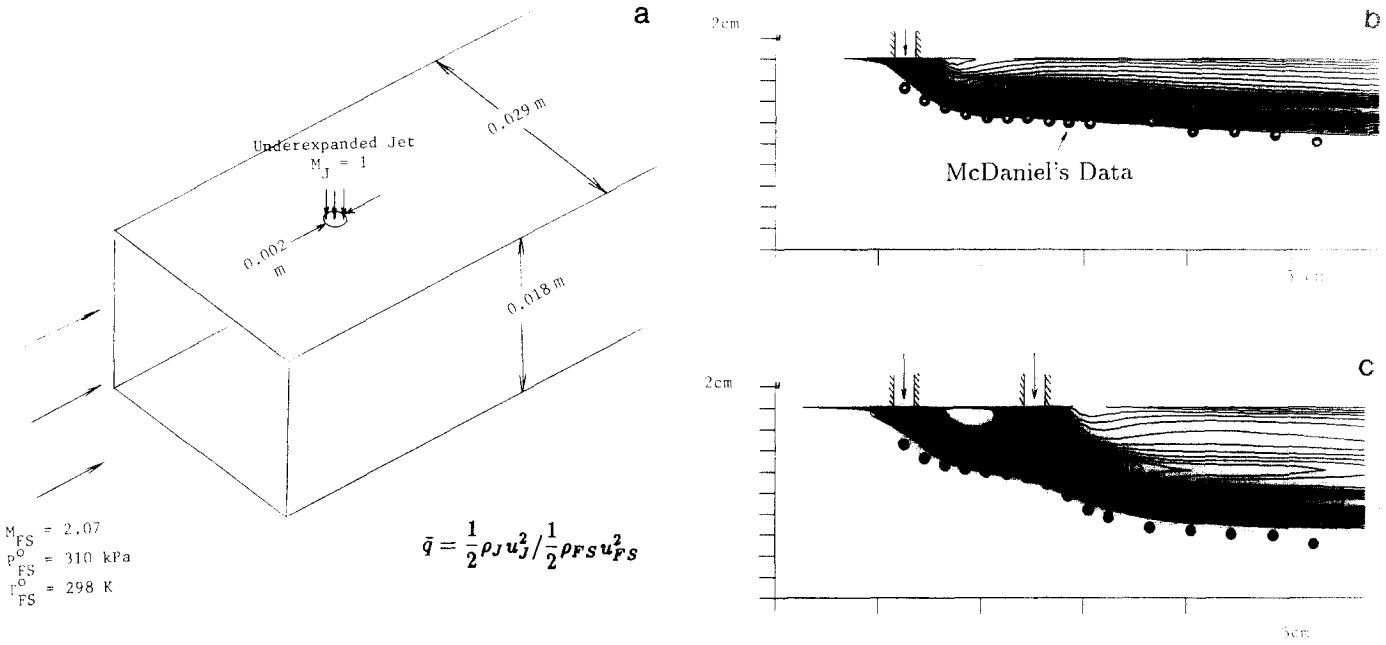

FIG. 2. McDaniel's Experiment: (a) geometry; (b) comparison of predicted and experimental jet penetration for single-port injection; (c) comparison of predicted and experimental jet penetration for dual-port injection.

RESULTS

To demonstrate the capability of the newly developed three-dimensional code, numerical examples of a transverse jet interacting with supersonic cross-flow are calculated. This flow phenomenon is of great interest because it is relevant to the fuel injection and mixing problem in scramjet engines.

In the first example, the program is applied to simulate the supersonic non-reacting mixing experiment reported by McDaniel and Graves [4]. In this experiment, iodine seeded air simulated the fuel injected into a Mach 2 cross stream. The fuel penetration was then visualized by the laser-induced fluorescence of iodine. The edge of the fuel jet was determined photographically and compared with the contour plot of the mass fraction of 0.01 of the fuel jet. The configuration of the experiment is illustrated in Fig. 2a; the comparisons between the experimental data and the theoretical prediction for both one-hole injection and two-hole injection in the supersonic cross-flow are shown in Figs. 2b and 2c. The predicted results compared favorably with the experimental data in terms of the penetration depth of the injected fuel in the supersonic cross-flow.

The computer code is then applied to calculate the chemically reacting flow fields of H_2 transverse jets injected into a Mach 4 airstream. Two cases were calculated: a single-injection and a dual-injection as shown in Fig. 3. A square duct and nozzle holes compose the flow configuration, in which

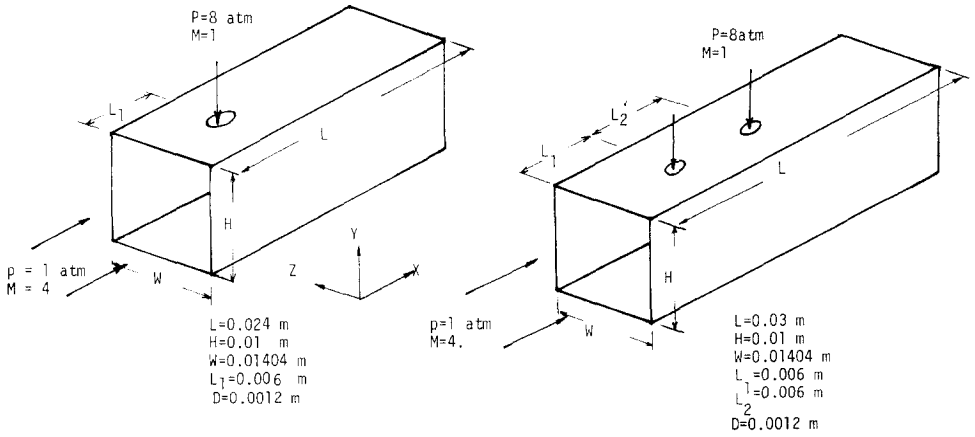

FIG. 3. Flow configurations.

the width is 1.404 cm and the height is 1 cm. The diameter of the injecting port is 0.12 cm. The injector is at the top wall of the duct and the injectant flows downward to interact with the cross-flow. For the single-hole injection case, the center of the injector orifice is located at a distance of five times of the diameter of the injecting orifice in the streamwise direction from the leading edge and one-half of the duct width in the cross direction. For the two-hole injection case, the first hole is located at the same position as the single-injection case. The second injecting port is at a distance of five diameters of the injecting port downstream from the first injecting port. The airstream is set to one atmosphere and 1300 K at the inlet. At the injection nozzle, the pressure is set at 8 atm, and the temperature is 700 K. No-slip and adiabatic conditions are used on the top wall. At the exit, the gradients of all variables in the streamwise direction are assumed to be zero. At both xy planes (where $z=0$ and $z=1.404$ cm) and at the bottom plane (the xz plane with $y=0$), the symmetric boundary conditions are imposed.

The convergence curves of the single injection case with three different grids are shown in Fig. 4. In about 5000 iterations, the residual of the coarse grid ($51\times21\times21$) calculation reduces about 10 orders of magnitude. For finer grids, numerical convergences slow down dramatically. In 5000 iterations, residuals reduce about five and six orders for fine ($101\times41\times41$) and medium ($71\times31\times31$) grids. This figure ensures us that the code indeed is very stable and can converge to the machine's limit. The results using the coarse grid are diffusive. However, insignificant differences were observed between the solutions of the fine and medium grids.

For the results shown in the following, for the single-injection case, the grid size is $63\times39\times43$ in the x, y, and z directions, respectively, and it took about 8 MW of memory on Cray 2. For the dual-injection case, the grid size is $81\times39\times43$ and the memory required was about 11 MW. The grid spacing is clustered in both the x direction and the z direction to resolve the injecting jet, while in the y direction the grid is clustered to resolve the wall boundary layers. For the present calculation, we stop the computation when the residuals reduced about four orders of magnitude; this criterion is sufficient for engineering purpose. The CPU time required for the single-injection case was about 5 h (grid size $63\times39\times43$) and that of the dual-injection case was about 6.5 h (grid size $81\times39\times43$).

Figures 5 and 6 shows the Mach number and temperature contours on the yz planes for various x locations. Just behind the injecting orifice, the Mach number contour shows a strong bow shock very close to the wall. Under the bow shock, the circular Mach number contour indicates the existence of the barrel shock structure. The jet has been bent and flows almost parallel to the primary flow. The penetration of the jet increases as the flow moves downstream. The

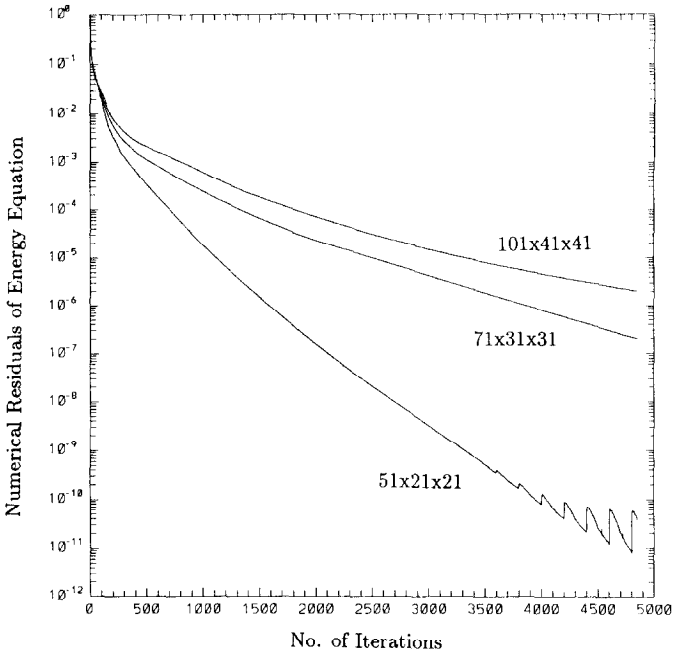

FIG. 4. Convergence history of the single injection case with three different grids.

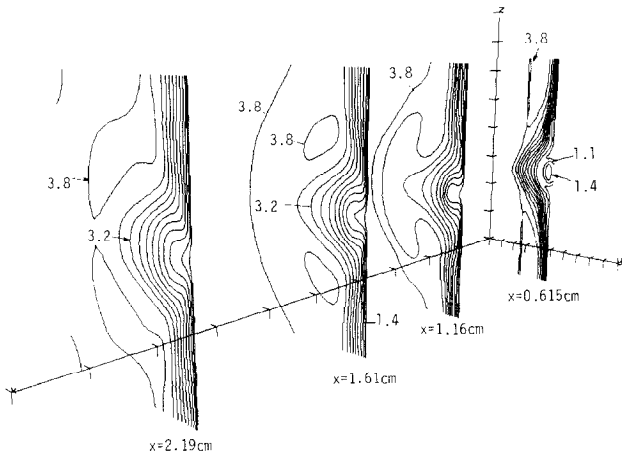

FIG. 5. Mach number contours on yz planes at various x locations for case 1.

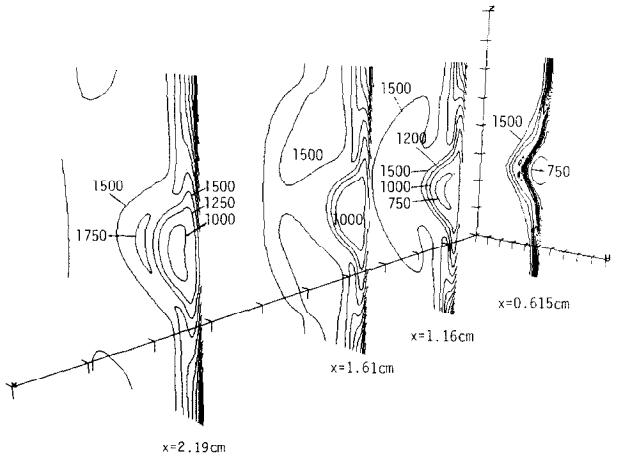

FIG. 6. Temperature contours on yz planes at various x locations for case 1.

shape of the jet also deforms as the flow moves downstream because streamwise vorticity is present in the lee of the injector. The secondary motion formed by two counterrotating vortices gives the bent-over jet a kidney shape. In the temperature contour plots, the hottest region is along the wall because of the viscous dissipation of the high speed flow enhanced by the combustion of H_2 and air. Away from the wall, comparing the Mach number plots and the temperature plots reveals that the temperature increases after the bow shock. Further downstream, a thin flame zone characterized by higher temperature develops.

Figures 7 and 8 depict the mass fraction contours of hydrogen and water. At the injecting orifice, the mass fraction of water is zero and that of hydrogen is one. Hydrogen diffuses into the airstream and consumed by chemical reaction as the jet flows downstream. Water is produced in the mixing layer between the jet and the airstream; a flame zone characterized by a high concentration of water can be cleary seen.

To give a thorough picture of the flow, contour plots in the xy plane across the orifice are also presented. Figure 9 shows the Mach number contours on the xy plane right at the center of the injecting port (cf. Fig. 3). Separated regions in front of the jet and in the lee of the jet which are mainly caused by the Prandtl–Meyer expansion of the underexpanded jet and by the blockage of the primary flow by the jet are clearly shown. In scramjet engines, these separation zones provide a longer fuel residence times as well as better-fuel-air mixing, resulting in a better flame holding capability of the combustor. Figure 10 illustrates the pressure contours on the xy plane. The jet partially blocks the supersonic cross-flow, resulting in a bow shock and a strong pressure gradient around the injector. In the wake region of the injector, a pressure deficit and relatively small gradients of streamwise velocity develop. The lower pressure in the wake induces a lateral inward motion, and very near the jet, a reverse flow occurs. Figure 11 shows the temperature contour on the xy plane. Again, the hottest region is along the wall. The flame zone extends from the hot region near the wall to the primary mixing zone between the fuel-rich core and cross-stream air.

Figure 12 shows the mass fraction contours of hydrogen. The recirculating flow in front of the injecting port entrains a large amount of hydrogen due to the Prandtl–Meyer expansion of the injected fuel. In the lee of the injecting port, hydrogen diffuses into the airstream and is consumed by the chemical reactions. But far downstream of the flow field, the core of the fuel jet still contains 50% of the fuel. This situation is greatly improved by adding one more fuel injection in the lee of the first injecting port. Figure 13 shows the mass fraction contour of water, which is the main product of the chemical reactions. Again, the flame zone is clearly discernible between the cold fuel jet and the hot airstream. The value of the water mass fraction in the flame zone varies

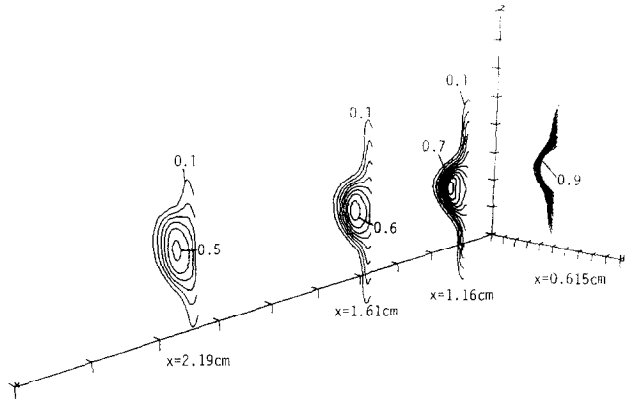

FIG. 7. Mass fraction of H_2 on yz planes at various x locations for case 1.

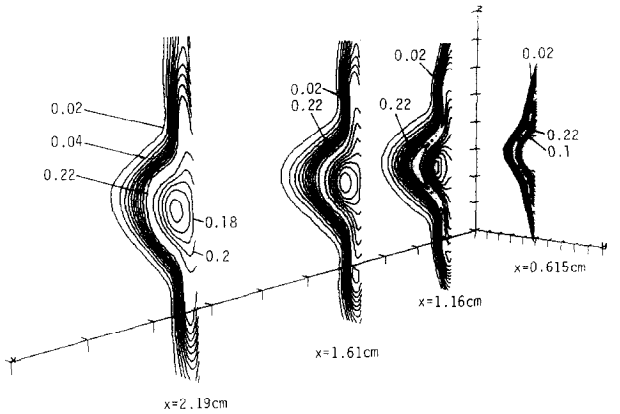

FIG. 8. Mass fraction of H_2O on yz planes at various x locations for case 1.

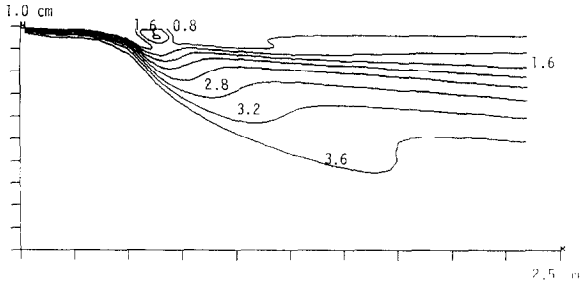

FIG. 9. Mach number contour on the xy plane at the center of the injection port for case 1.

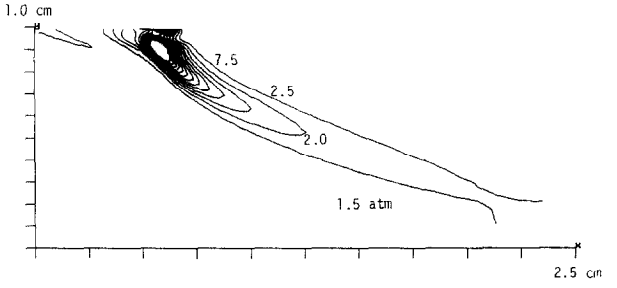

FIG. 10. Pressure contour on the xy plane at the center of the injection port for case 1.

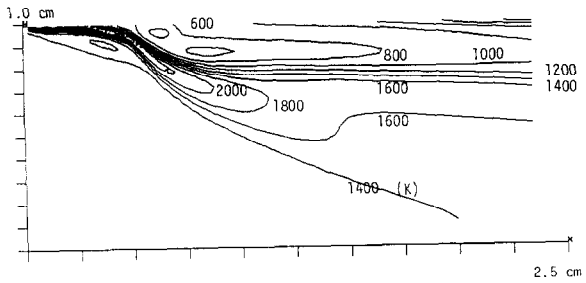

FIG. 11. Temperature contour on the xy plane at the center of the injection port for case 1.

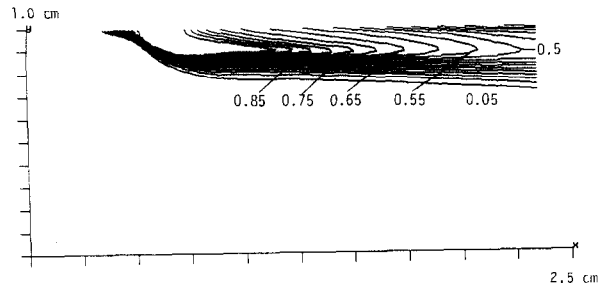

FIG. 12. Mass fraction of H_2 on the xy plane at the center of the injection port for case 1.

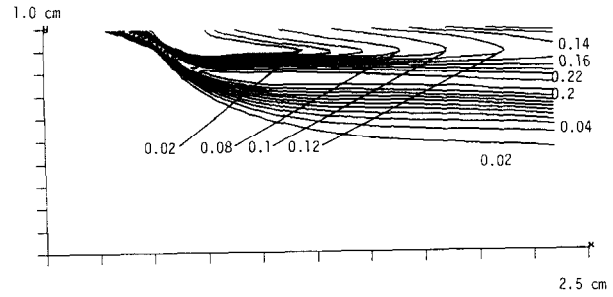

FIG. 13. Mass fraction of H_2O on the xy plane at the center of the injection port for case 1.

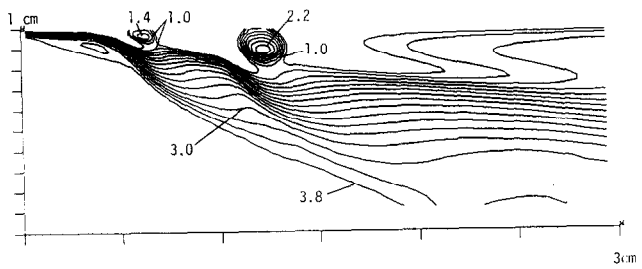

FIG. 14. Mach number contour on the xy plane at the center of the injection port for case 2.

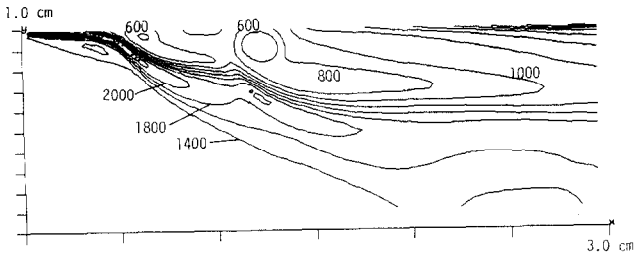

FIG. 15. Temperature contour on the xy plane at the center of the injection port for case 2.

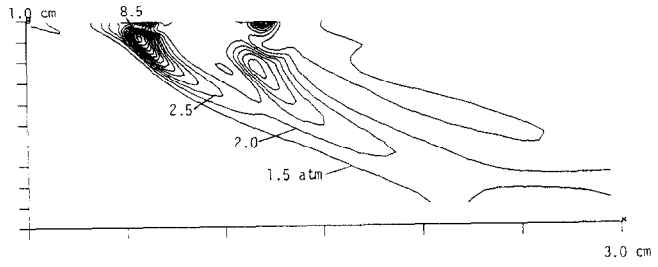

FIG. 16. Pressure contour on the xy plane at the center of the injection port for case 2.

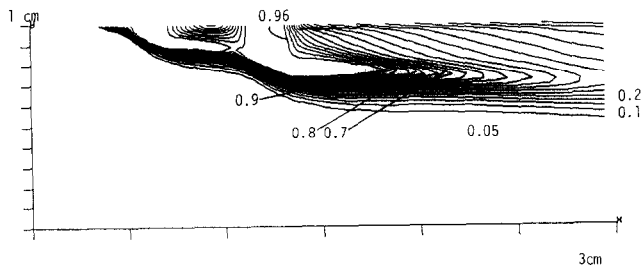

FIG. 17. Mass fraction of H_2 on the xy plane at the center of the injection port for case 2.

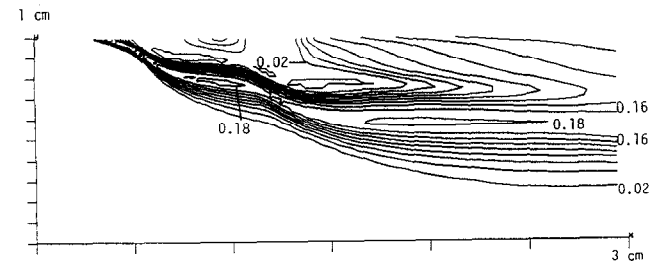

FIG. 18. Mass fraction of H_2O on the xy plane at the center of the injection port for case 2.

between 0.22 to 0.25. Although not shown, the amount of the intermediate species OH was relatively high in the flame zone, indicating the characteristic time for chemical reaction is comparable to the flow residence. Thus, the flow does not reach chemical equilibrium.

Figures 14 to 18 shows the solutions of the dual-injection case. Similar physical features of the flow around the first port were observed. However, because the first fuel jet blocks the main airstream, the second fuel jet experiences a much stronger expansion, as seen in the Mach number, pressure, and temperature contours. Thus, hydrogen from the second injecting port has a much better chance penetrating into the cross airstream. Also note that the flow field between the two injecting ports and the area just inside the lee of the second port are largely subsonic and recirculating. These regions are particularly interesting and can be responsibe for flame holding and fuel–air mixing.

CONCLUDING REMARKS

A new three-dimensional code using an LU scheme for calculating chemically reacting flows in scramjets has been developed. Detailed physical models simulating chemical reactions and gas mixture for supersonic reacting flows has been incorporated. The program is efficient and robust, particularly for three-dimensional calculations. The code has been tested by calculating the non-reacting binary mixing of a sonic jet transversely injected into a supersonic cross-flow. The penetration depth of fuel jet predicted by the code compared favorably with experimental data. The code is then applied to simulate the chemically reacting flow field of an underexpanded hydrogen jet transversely injected into a supersonic hot airstream. The results clearly depicted the shock structure, recirculation region, and the flame zone. In the dual-injection case, because the first jet blocks the primary flow, the second jet can penetrate deeper into the airstream and has more complete combustion.

REFERENCES

1. S. Yoon and A. Jameson, *AIAA J.* **25**, 929 (1989).
2. J. S. Shuen and S. Yoon, *AIAA J.* **27**, 1752 (1989).
3. S. T. Yu, B. J. McBride, K. C. Hsieh, and J. S. Shuen, "Numerical Simulation of Hypersonic Inlet Flows with Equilibrium or Finite Rate Chemistry," AIAA Paper 88-0273, 1988 (unpublished).
4. J. C. McDaniel and J. Graves, Jr., "A Laser-Induced Fluorescence Visualization Study of Transverse, Sonic Fuel Injection in a Non-reacting Supersonic Combustor," AIAA Paper 86-0570, 1986 (unpublished).
5. F. A. Williams, *Combustion Theory* (Benjamin/Cummings, New York, 1985), p. 634 and p. 585.
6. S. Gordon and B. J. McBride, "Computer Program for the Calculation of Complex Equilibrium Compositions, Rocket Performance, Incident and Reflected Shocks, and Chapman–Jouguet Detonations," NASA SP-273, 1976 (unpublished).
7. R. C. Reid, J. M. Prausnitz, and B. E. Poling, *The Properties of Gases and Liquids* (McGraw–Hill, New York, 1988), p. 407 and p. 581.
8. T. A. Brabbs, Internal Fluid Mechanics Division, NASA Lewis Research Center, Cleveland, OH, private communication (1988).
9. B. S. Baldwin and H. Lomax, "Thin Layer Approximation and Algebraic Model for Separated Turbulent Flows," AIAA Paper 78-257, 1978 (unpublished).
10. T. R. Bussing and E. M. Murman, "A Finite Volume Method for the Calculation of Compressible Chemically Reacting Flows," AIAA Paper 85-0331, 1985 (unpublished).
11. D. K. Prabhu and J. C. Tennehill, *J. Spacecraft* **23**, 264 (1986).
12. P. Colella and H. M. Glaz, *J. Comput. Phys.* **59**, 264 (1985).
13. A. Jameson and E. Turkel, *Math. Comput.* **37**, 385 (1981).
14. R. Beam and R. F. Warming, *J. Comput. Phys.* **22**, 87 (1976).